Title
Estimation of surface longwave radiation components from ground-based historical net radiation and weather data

Journal
Journal of Geophysical Research Atmospheres, 113(4)

ISSN
0148-0227

Authors
Park, GH
Gao, X
Sorooshian, S

Publication Date
2008-02-27

DOI
10.1029/2007JD008903

Estimation of surface longwave radiation components from ground-based historical net radiation and weather data

Gi-Hyeon Park,[1] Xiaogang Gao,[1] and Soroosh Sorooshian[1]

Received 2 May 2007; revised 10 September 2007; accepted 16 November 2007; published 22 February 2008.

[1] A methodology for estimating ground upwelling, clear-sky and cloud downwelling longwave radiations ($L^{\uparrow}$, $L^{\downarrow}_{sky}$, and $L^{\downarrow}_{cld}$) and net shortwave radiation (S_n) at 30-min temporal scales based on long-term ground-based net radiations and meteorological observations is described. Components of surface radiation can be estimated from empirical models, cloud radiation models, and remote sensing observations. The proposed method combines the local calibration of empirical models and the radiative energy balance method to obtain the dual-directional, dual-spectral components of the surface radiation for the offline land surface process modeling and ecosystem study. By extracting information of radiation components from long-term net radiation and concurrent weather data, the utility of tower net radiation observations is maximized. Four test sites with multiyears' radiation records were used to evaluate the method. The results show that when compared with the results of empirical models using default parameters the proposed method is able to produce more accurate estimates of longwave surface components ($L^{\uparrow}_{g}$, $L^{\downarrow}_{sky}$, $L^{\downarrow}_{cld}$) and net shortwave radiation (S_n). Overall, the estimated and observed surface radiation components show high correlations (>0.90), high index of agreement (>0.89), and low errors (root mean square error <30 W m^{-2} and bias <11 W m^{-2}) at all of the test sites. The advantage of this scheme is that the refinement is achieved using the information from the historical net radiation and weather data at each observation site without additional measurements. This method is applicable for many existing observation sites worldwide which have long-term (at least 1 year) continuous net radiation records.

Citation: Park, G.-H., X. Gao, and S. Sorooshian (2008), Estimation of surface longwave radiation components from ground-based historical net radiation and weather data, *J. Geophys. Res.*, *113*, D04207, doi:10.1029/2007JD008903.

1. Introduction

[2] Surface net radiation (R_n) is the major energy forcing that drives many land surface processes such as evapotranspiration and photosynthesis. As formulated in the land surface schemes, downward components of surface net radiation, i.e., incoming shortwave ($S^{\downarrow}$) and incoming thermal ($L^{\downarrow}$) radiations, possess different partitions at the soil and plant surfaces. Therefore site measurements of downwelling surface radiations in shortwave and longwave spectrums ($S^{\downarrow}$ and $L^{\downarrow}$) are essential for better simulation and understanding of land surface processes.

[3] Over the past decade, many ground measurement sites have been set up and abundant data have become available to support diverse interdisciplinary researches for validations of land surface modeling, remote sensing estimation, and ecosystem studies. However, except for the programs designed specifically for radiation and cloud studies such as the U.S. Department of Energy's Atmospheric Radiation Measurement (ARM) program, most ground tower sites measure either only R_n or R_n with $S^{\downarrow}$. In other words, downwelling longwave radiations are often unmeasured from the flux towers. For example, the global cooperative micrometeorological flux measurement project, FLUXNET (http://www-eosdis.ornl.gov/FLUXNET/) is a global network of several regional to continental networks (e.g., AmeriFlux, CarboEurope, Asiaflux, KoFlux, OzFlux, Fluxnet-Canada, and ChinaFlux) and included hundreds of observation sites worldwide that provide many years' continuous tower measurements of carbon dioxide, water, energy, and momentum at 30–60 min time intervals. These long-term data covering a wide range of climates and geography are useful to verify the results of General Circulation Models and land surface models. However, only a small number of the FLUXNET sites (23 sites among 123 AmeriFlux sites) provides the data including various radiation components, i.e., upwelling and downwelling shortwave and longwave radiations ($S^{\uparrow}$, $S^{\downarrow}$, $L^{\uparrow}$, and $L^{\downarrow}$). Because the major goal of this study is to maximize the utilization of existing flux tower observations for the offline land surface modeling and ecosystem studies, it is critical to find an appropriate procedure to estimate the needed radiation

[1]Department of Civil and Environmental Engineering, University of California, Irvine, California, USA.

0148-0227/08/2007JD008903

Table 1. Site Description

Site	Land Class	Location	Elevation, m	Study Period
Willow Creek, WI	hardwood	45°48′21″N/90°05′48″W	515	1 Jan 1998 to 31 Dec 2002
Niwot Ridge, CO	mixed forest	40°01′58″N/105°32′7″W	3,050	1 Jan 1999 to 31 Dec 2003
Fort Peck, MT	flat grassland	48°18′28″N/105°06′02″W	634	1 Jan 2000 to 25 Jun 2005
Audubon, AZ	semiarid desert	31°35′27″N/110°30′37″W	985	7 Jun 2002 to 5 Mar 2005

components for the measurement sites where they are not separately measured.

[4] Many studies have dealt with the estimation of S_n components through satellite remote sensing [*Gautier et al.*, 1980; *Pinker and Ewing*, 1985; *Pinker and Laszlo*, 1992; *Platnick and Fontenla*, 2008; *Tarpley*, 1979], radiative transfer modeling [*Bird*, 1984; *Leckner*, 1978] and parameterization of the empirical models [*Ångström*, 1924; *Bechini et al.*, 2000; *Ehnberg and Bollen*, 2005; *Iqbal*, 1979; *Yang and Koike*, 2005]. Daily biases of the surface solar radiation estimated from the visible and near-infrared satellite observations are reported to be less than 10% [*Gautier and Landsfeld*, 1997]. *Rigollier et al.* [2004] summarized the accuracy of solar radiation of the method Hellios-1, which shows that biases of hourly irradiance are −1% to 10% and RMSE ranges from 14% to 30%. *Long and Ackerman* [2000] developed a method to determine clear sky periods from 1-min measurements of downwelling and diffuse shortwave radiations. However, this method cannot be used for most existing tower data sets because of the unavailability of the additional measurements at the tower sites. Although satellite remote sensing of shortwave radiation has been of great interest, ground observations are still required to verify the accuracies and the suitability of its products for the offline land surface studies at diverse environments.

[5] Surface longwave radiations are less studied and understood than surface shortwave radiation. *Wild and Cechet* [2002] mentioned that downwelling sky longwave radiation as the only component that is not well understood on global basis. In common practice, surface longwave radiations are estimated from empirical models. Empirical models are formulated on the basis of the regression of observed radiation and weather data at particular locations. Therefore substantial errors due to the applications of the empirical models beyond their observation sites have been addressed in many previous studies [*Kimball et al.*, 1982; *Pirazzini et al.*, 2001], which predicates the need of local calibration of these models at each location. In the similar case of using empirical model to estimate surface shortwave radiation, *Yang and Koike* [2005] pointed out that one of the sunshine-based empirical solar radiation models (Ångström model) needs calibrations for the local regions. Alternatively, $L^{\downarrow}$ data can be provided through numerical model or reanalysis (such as *Mesinger et al.* [2006]), but the data accuracy may be questionable because cloud simulation is one of the major weaknesses of current meteorological models. The empirical models are expected to continue being the common approaches to estimate surface longwave radiations until more accurate models or remote sensing techniques are developed.

[6] In this study, we propose a method to improve the estimation accuracy of the longwave components by adding information from long-term net radiation observations, which then leads to the estimation of surface net shortwave radiation. Section 2 provides information relevant to the radiation measurements used in this study. Section 3 describes the procedure to estimate longwave components and net shortwave radiation, and section 4 evaluates and discusses the results at four test sites. Conclusions and discussions are presented in section 5.

2. Data

2.1. AmeriFlux Tower Observations

[7] The surface spectral radiation data of field observations analyzed in this study are from four AmeriFlux sites in the United States. They are Willow Creek in Wisconsin, Niwot Ridge in Colorado, Fort Peck in Montana, and Audubon in Arizona. The basic reasons for this selection are (1) the availability of continuous field measurements spanning over multiple years at these sites and (2) the availability of four radiation components (i.e., $S^{\downarrow}$, $S^{\uparrow}$, $L^{\downarrow}$, and $L^{\uparrow}$) in addition to R_n for the validation of the proposed method. These long-term, dual-spectral and dual directional measurements provide a unique opportunity for the development and validation of the statistical scheme that estimate spectral radiation components solely from net radiation observations and concurrent weather data. The data downloaded from the AmeriFlux website at these stations are the level 2 data at 30-min temporal intervals (not the ''gap-filled'' data which currently have short record periods at limited sites). Table 1 represents the geographic locations of the four sites. The time period studied at each site is around 3–5 years. This selection was made in order to examine the developed estimation scheme on a long-term multisite observation basis.

[8] The four sites are instrumented with Kipp and Zonen CNR1 radiometers and radiations are measured at a frequency of 1 Hz with sensors mounted on the instrument towers. Four individual sensors are used to measure incoming and reflecting shortwave radiations ($S^{\downarrow}$ and $S^{\uparrow}$) in the spectral range between 305 and 2,800 nm, and incoming and emitted thermal radiations ($L^{\downarrow}$ and $L^{\uparrow}$) in the spectral range between 5,000 and 50,000 nm.

2.2. GCIP/GAP SRB Cloud Cover Fraction

[9] The GOES Cloud cover fraction data are used to evaluate the estimated clear sky downwelling longwave radiation ($\hat{L}^{\downarrow}_{sky}$). They are produced from GOES visible images and are available from Surface Radiation Budget (SRB) Data of the GEWEX Continental Scale International Project (GCIP) and GEWEX Americas Prediction Project (GAPP). The 0.5° resolution cloud cover fraction data were obtained online (http://www.atmos.umd.edu/~srb/gcip/webgcip.htm) and 1.5° × 1.5° cloud cover fractions centering at the four AmeriFlux sites were calculated and used

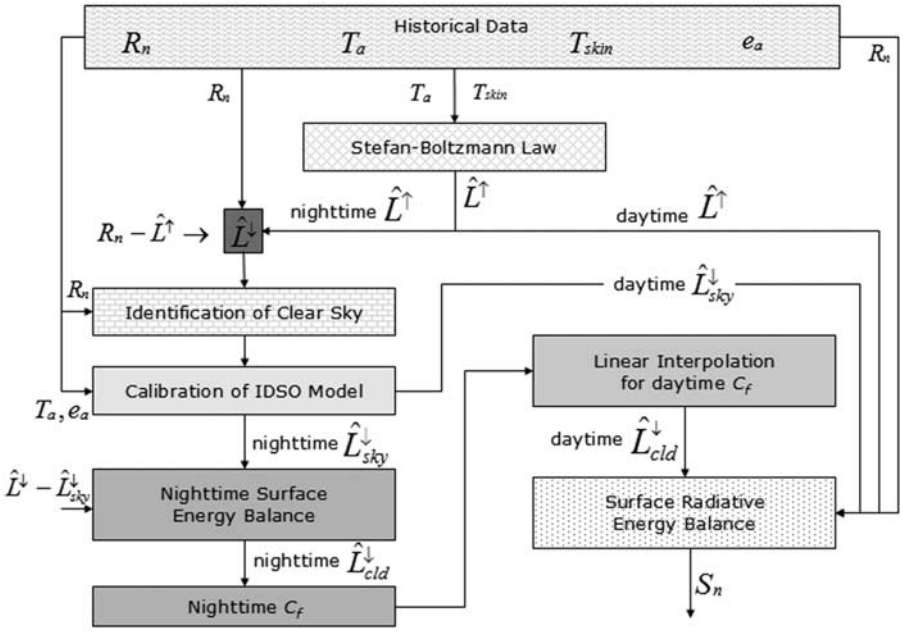

Figure 1. Flowchart of the surface radiation component estimation method.

to define clear sky conditions. Since GOES cloud fraction data do not provide cloudiness information during nighttime, the data are only used to evaluate daytime $\hat{L}^{\downarrow}_{sky}$.

3. Method

[10] Surface net radiation (R_n, counted positively downward) is defined as the summation of net shortwave radiation (S_n) and net longwave radiation (L_n). In this study, we focus on estimating the L_n components, while calculating S_n as the residual term of the surface radiation balance. The L_n consists of three components: (1) clear sky downwelling radiation ($L^{\downarrow}_{sky}$) emitted by various atmospheric composites except clouds, (2) cloud downwelling radiation ($L^{\downarrow}_{cld}$), and (3) ground upwelling longwave radiation ($L^{\uparrow}$). Thereby, the radiation balance at land surface is presented as:

$$R_n = S_n + L_n = S_n + L^{\downarrow}_{sky} + L^{\downarrow}_{cld} - L^{\uparrow} \quad (1)$$

[11] The goal of the study is to partition R_n into its components (i.e., the right hand terms of equation (1)) using meteorological observations. Figure 1 is a flowchart that depicts the processing steps of the method to estimate the surface radiation components. The method first estimates upwelling ground longwave radiations, which then are subtracted from the nighttime net radiation to estimate the nighttime downwelling longwave radiations (i.e., nighttime $\hat{L}^{\downarrow}_{sky} + \hat{L}^{\downarrow}_{cld}$). From the long-term nighttime data, the empirical clear-sky longwave radiation model is calibrated to the lower mode of the estimated nighttime longwave radiations. An empirical single-layer cloud sky longwave radiation model is then used to extract the cloud information during nighttime, and then the daytime cloud properties are linearly interpolated. Total surface downwelling longwave radiations are estimated by combining the estimated clear-sky and cloud downwelling longwave radiations. Details of each procedure are further described in the following sections.

3.1. Estimation of Ground Upwelling Longwave Radiation ($\hat{L}^{\uparrow}$)

[12] $L^{\uparrow}$ is governed by the Stefan-Boltzmann Law as:

$$L^{\uparrow} = \varepsilon_g \sigma T^4_{skin} \quad (2)$$

where $\varepsilon_g \approx 0.95 \sim 1.0$ is the bulk emissivity of land surface, σ is the Stefan-Boltzmann constant and T_{skin} is the surface skin temperature defined as the equivalent or effective temperature responsible for the longwave emission from a heterogeneous land surface. T_{skin} can be measured by radiometers or Infrared Thermocouple Sensors (IRTS) mounted on towers or estimated by satellite remote sensing under clear sky conditions. However, skin temperature measurements (either from IRTS or satellites) are only available at a few measurement sites. In practice, surface air temperature T_a (at 2-m height) can be used as its substitute for the specific types of land surfaces such as dense vegetated area, where temperature difference between land surface and air above it is not significantly large. Error in $\hat{L}^{\uparrow}_a$ calculated from T_a is discussed in the result section.

3.2. Estimation of Clear-Sky Downwelling Longwave Radiation ($\hat{L}^{\downarrow}_{sky}$)

[13] $L^{\downarrow}_{sky}$ is the longwave radiation emitted by atmospheric composites except for clouds. Among many empirical models (see the review of *Iziomon et al.* [2003]), this study uses the IDSO empirical model [*Idso*, 1981; *Kimball et al.*, 1982] adopted by land surface models (for example, Common Land model (Y. Dai et al., Common Land Model (CLM), technical documentation and user's guide, available at http://climate.eas.gatech.edu/dai/clmdoc.pdf)). Similar to many others, IDSO empirical model represents $L^{\downarrow}_{sky}$ as a

function of surface air temperature (T_a) and vapor pressure (e_a) based on field measurements: $L^{\downarrow}_{sky} = f(T_a, e_a)$. Since empirical models were developed on the basis of a few ground observation sites, they tend to show greater errors in other sites. In order to improve the accuracy of empirical model estimations, it is necessary to calibrate the model parameters on the basis of the data from the applied location.

[14] A procedure to extract $L^{\downarrow}_{sky}$ from R_n and weather data is addressed as follows. First, it is necessary to separate clear-sky hours from all-sky observations. *Long and Ackerman* [2000] developed a method to separate clear-sky hours using observed broadband solar radiations, which are however unavailable at most of existing tower sites. Clear sky conditions can also be identified through cloudiness data from ground observations by trained observer, total sky imager (TSI), and satellite remote sensing. However, most measurement sites do not collect cloudiness data at 30-min interval. Our choice for the separation of local $L^{\downarrow}_{sky}$ is to use the observed nighttime downward longwave radiation ($\hat{L}^{\downarrow}$) and weather data (T_a and relative humidity), since during nighttime $L^{\downarrow}_{sky}$ is the only LW downwelling component under clear-sky conditions ($L^{\downarrow}_{cld} = 0$). During nighttime, according to equation (1), we have $S_n = 0$, $R_n = L^{\downarrow}_{sky} + L^{\downarrow}_{cld} - L^{\uparrow}$ or $L^{\downarrow}_{sky} + L^{\downarrow}_{cld} = R_n + L^{\uparrow}$. Here, R_n is given and $L^{\uparrow}$ can be replaced with the upwelling ground longwave radiation ($\hat{L}^{\uparrow}_a$ or $\hat{L}^{\uparrow}_{skin}$) estimated from the concurrent T_a or T_{skin} through the above procedure. Therefore the nighttime all sky downward radiation ($\hat{L}^{\downarrow} = \hat{L}^{\downarrow}_{sky} + \hat{L}^{\downarrow}_{cld}$) at each site can be extracted from the R_n and $\hat{L}^{\uparrow}$. Next, we distribute the nighttime ($\hat{L}^{\downarrow} = \hat{L}^{\downarrow}_{sky} + \hat{L}^{\downarrow}_{cld}$) data into bins in the (T_a, e_a) coordinate plane according to their (T_a, e_a) values. We divided them into 30 × 30 bins for this study to capture the variability of $\hat{L}^{\downarrow}$ in the (T_a, e_a) space and also to allow each bin to have enough number of samples. Each (T_a, e_a) bin collects a large number of nighttime ($\hat{L}^{\downarrow} = L^{\downarrow}_{sky} + L^{\downarrow}_{cld}$) data (different $\hat{L}^{\downarrow}$ values under the same (T_a, e_a) but distinct cloud conditions). Because under clear-sky conditions ($L^{\downarrow}_{cld} = 0$) the $\hat{L}^{\downarrow}$ will be less than under cloud-sky conditions at the same (T_a, e_a) bin, we then find the mode of the lower 50 percentile of $\hat{L}^{\downarrow}$ as the representative value of $L^{\downarrow}_{sky}$ for each bin (note that the values of $L^{\downarrow}_{sky}$ in a ($T_a - e_a$) bin are not a fixed value but in a range). These data points are further filtered with a threshold to ensure a sufficient number of data within each bin. The threshold is set to be 0.2% of the total number of data. Notice that the observed $L^{\uparrow}$ and $L^{\downarrow}$ from the test sites are not used in this procedure, they are only used for verification.

[15] The extracted nighttime $\hat{L}^{\downarrow}_{sky}$ data are then used to calibrate the parameters of an empirical mode. In this study, the IDSO model [*Idso*, 1981] is selected:

$$\hat{L}^{\downarrow}_{sky} = \sigma T_a^4 [A + B \cdot e_a \cdot Exp(C/T_a)] \tag{3}$$

where e_a is the vapor pressure in kPa and A, B, and C are model parameters which need to be calibrated. This model was originally regressed from the observational data at Phoenix, Arizona [*Idso*, 1981] and later checked at Sydney, Australia by *Kimball et al.* [1982]. The model was selected for this study because it has been adopted by many LSMs, such as the recently developed Common Land Model (Y. Dai et al., Common Land Model (CLM), technical documentation and user's guide, available at http://climate.eas.gatech.edu/dai/clmdoc.pdf). By using the optimization scheme of Shuffled Complex Evolution [*Duan et al.*, 1992], a new set of parameters (i.e., A, B, and C) for each test site that best fits its nighttime $L^{\downarrow}_{sky}$ data can be obtained. The Idso model (i.e., equation (3)) with the locally calibrated parameters was employed to calculate 30-min $\hat{L}^{\downarrow}_{sky}$ for both daytime and nighttime.

3.3. Estimation of Cloud Downwelling Longwave Radiation ($\hat{L}^{\downarrow}_{cld}$)

[16] We have discussed so far the procedures to calculate $\hat{L}^{\uparrow}$ (either from T_a or T_{skin}) and $\hat{L}^{\downarrow}_{sky}$ from historical R_n and weather data. For nighttime ($S_n = 0$), the third LW components $L^{\downarrow}_{cld}$ can now be calculated according to the surface radiation balance ($L^{\downarrow}_{cld} = R_n + L^{\uparrow} - L^{\downarrow}_{sky}$). We only replace $L^{\uparrow}$ and $L^{\downarrow}_{sky}$ with our estimated values ($\hat{L}^{\uparrow}$ and $\hat{L}^{\downarrow}_{sky}$) obtained from the previous procedures. During daytime, because of the high variability of clouds, quantitative description of cloudiness and cloud effects on surface radiations including solar diffusion and attenuation and LW emission is difficult and remains as one of the high priorities for radiation and cloud research projects. In this study, *Steiner*'s [2001] single-layer empirical model that was suggested on the basis of the multilayer cloud radiation model of *Kimball et al.* [1982] is employed (more detailed description about these two models can be found in Appendix A):

$$L^{\downarrow}_{cld} = \tau_8 A_c \varepsilon_c f_8 \sigma T_c^4 \tag{4}$$

where T_c is the cloud effective temperature that can be estimated from T_a and e_a; τ_8, f_8, σ are physical constants (see Appendix A); cloudiness A_c and cloud bulk emissivity ε_c are related to the cloud properties and cloud vertical and horizontal distribution. Because of the difficulty of retrieving daytime cloud information from the historical R_n and weather data, we introduce an integrated cloud factor: $C_f = A_c \varepsilon_c$, so that equation (4) becomes:

$$L^{\downarrow}_{cld} = C_f \tau_8 f_8 \sigma T_c^4 \tag{5}$$

As mentioned above, during nighttime, $\hat{L}^{\downarrow}_{cld} = R_n + \hat{L}^{\uparrow} - \hat{L}^{\downarrow}_{sky}$ can be calculated from observed R_n, and estimated $\hat{L}^{\uparrow}$ and $\hat{L}^{\downarrow}_{sky}$. Therefore, at two special nighttimes, (1) just before the start of a local daytime and (2) just after the end of the daytime, the C_f values can be calculated. We then propose to linearly interpolate these two calculated C_f values during daytime. It must be mentioned that this assumption clearly contains some limitation and introduces errors. In summary, of the four factors in equation (5), C_f is the only one that is obtained through interpolation (as explained above). The other factors (τ_8, f_8, and T_c) are estimated from daytime meteorological observations, that contain information of atmospheric and cloudiness condition.

3.4. Estimation of All-Sky Downwelling Longwave Radiation ($\hat{L}^{\downarrow}$)

[17] All-sky downwelling longwave radiation ($\hat{L}^{\downarrow}$) is simply the sum of the estimated clear-sky downwelling longwave radiation ($\hat{L}^{\downarrow}_{sky}$) and the estimated cloud down-

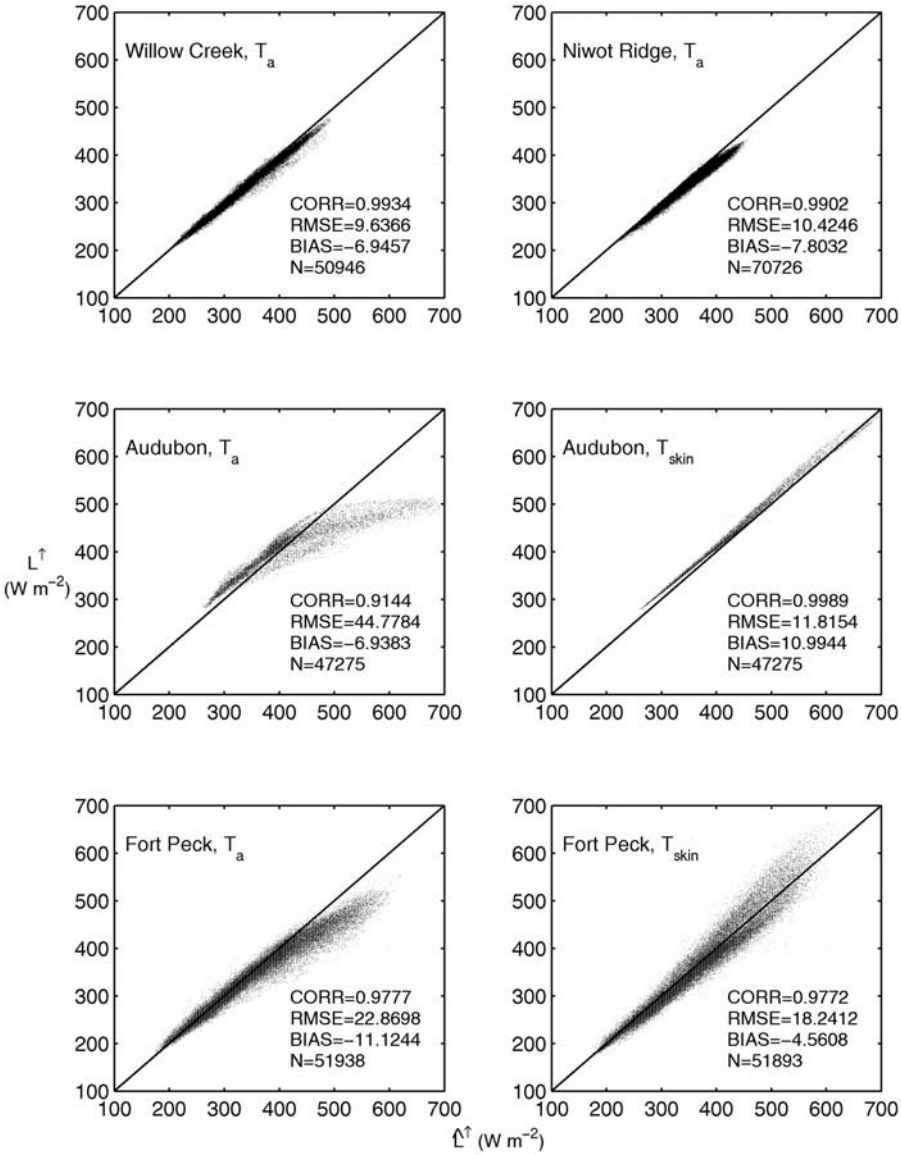

Figure 2. Comparison of $\hat{L}^{\uparrow}$ (estimation) and $L^{\uparrow}$ (observation) at the test sites (N for the number of data points). Notice that T_{skin} data are available at Audubon and Fort Peck; therefore the $\hat{L}^{\uparrow}$ estimated using T_a and T_{skin} are plotted.

welling longwave radiation ($\hat{L}^{\downarrow}_{cld}$). However, $\hat{L}^{\downarrow}$ is equal to ($R_n - \hat{L}^{\uparrow}$) during the nighttime.

3.5. Estimation of Net Solar Radiation ($\hat{S}_n$)

[18] Once all the LW radiation components are estimated, surface net solar radiation ($\hat{S}_n$) is estimated as the residual term of the land surface radiation balance ($\hat{S}_n = R_n - \hat{L}^{\downarrow}_{sky} - \hat{L}^{\downarrow}_{cld} + \hat{L}^{\uparrow}$). Net solar radiation is the most important energy source that drives many land surface processes. Separating S_n from R_n is a key step to expand the utility of the historical data to interdisciplinary studies. In order to further partition $\hat{S}_n$ into $S^{\uparrow}$ and $S^{\downarrow}$, 30-min data of albedo are required for each site. However, this is beyond the scope of this paper.

4. Results and Discussions

[19] Our comparisons follow the same order in the procedure, starting from $\hat{L}^{\uparrow}$, $\hat{L}^{\downarrow}_{sky}$, $\hat{L}^{\downarrow}$ ($=\hat{L}^{\downarrow}_{sky} + \hat{L}^{\downarrow}_{cld}$) to $\hat{S}_n$. Correlation Coefficient (Corr), Mean bias (BIAS), Root Mean Square Error (RMSE), and Willmott's index of agreement (W_{IA}) [*Willmott*, 1982] were used as the statistical measures to evaluate the method suggested.

4.1. Evaluation of Estimated Ground Upwelling Emission ($\hat{L}^{\uparrow}$)

[20] In Figure 2, the observed $L^{\uparrow}$ at the test sites are compared with $\hat{L}^{\uparrow}$ estimated from either T_a or T_{skin} (where the observed T_{skin} are available). The two $\hat{L}^{\uparrow}$ from T_a and T_{skin} are denoted as $\hat{L}^{\uparrow}_a$ and $\hat{L}^{\uparrow}_{skin}$, respectively. Over the three vegetated sites (Willow Creek: Hardwood, Niwot Ridge: Mixed forest, and Fort Peck: Grassland), $\hat{L}^{\uparrow}_a$ is close to the observed $L^{\uparrow}$ with correlation (Corr) greater than 0.97, Root Mean Square Error (RMSE) less then 23 W m^{-2}, and bias less than -10 W m^{-2}. The bias becomes slightly more negative in the high range of $L^{\uparrow}$ (>400 W m^{-2}). Over the

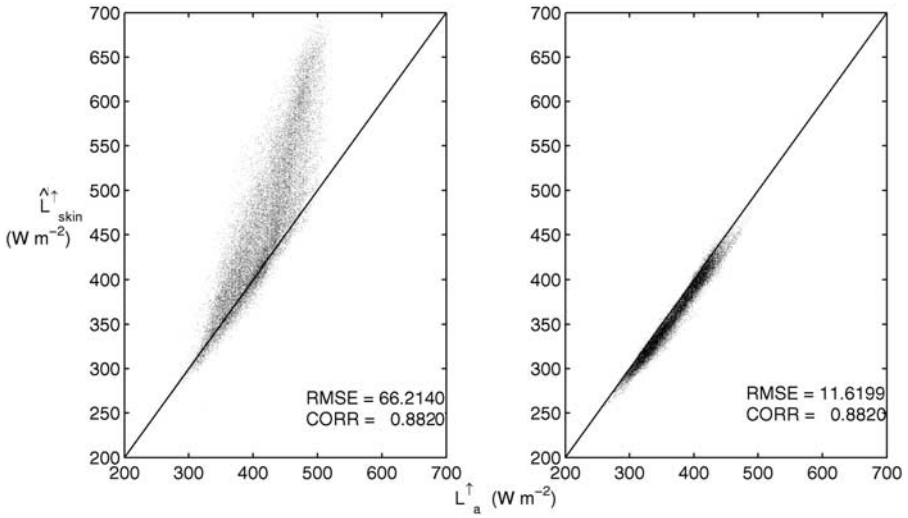

Figure 3. Comparison of $L^{\uparrow}$ estimates using T_a and T_{skin} at Audubon, AZ for (left) daytime data and (right) nighttime data.

semiarid site of Audubon, AZ, the high-range negative bias becomes substantial but disappears when the skin temperature is used. The skin temperature reported from the field sites are the direct measurements from the Infrared Thermocouple Sensor (IRTS) installed on the tower at the two sites (Fort Peck and Audubon), although it could also be calculated from the observed $L^{\uparrow}$. Investigations for the data points with large negative biases (Figure 3) indicate that the

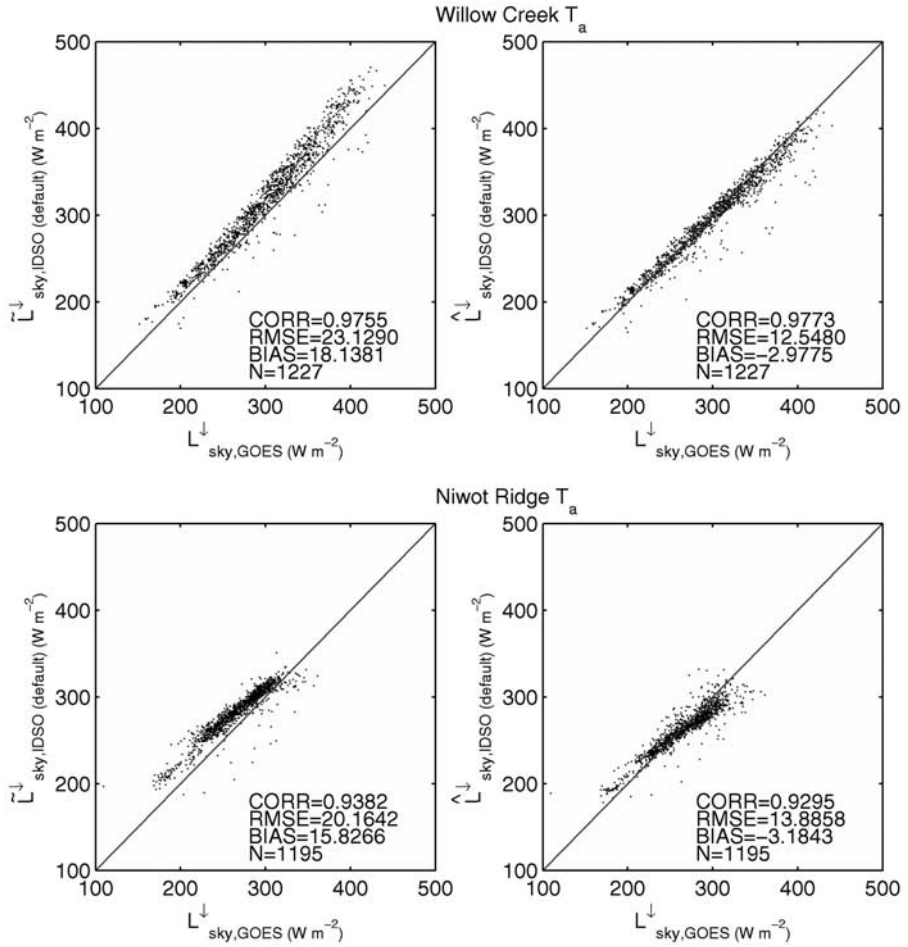

Figure 4. Comparison of $\tilde{L}^{\downarrow}_{sky}$ and $\hat{L}^{\downarrow}_{sky}$ (using the published and calibrated model parameters, respectively) with the observed GOES clear-sky conditions at the sites without T_{skin} data.

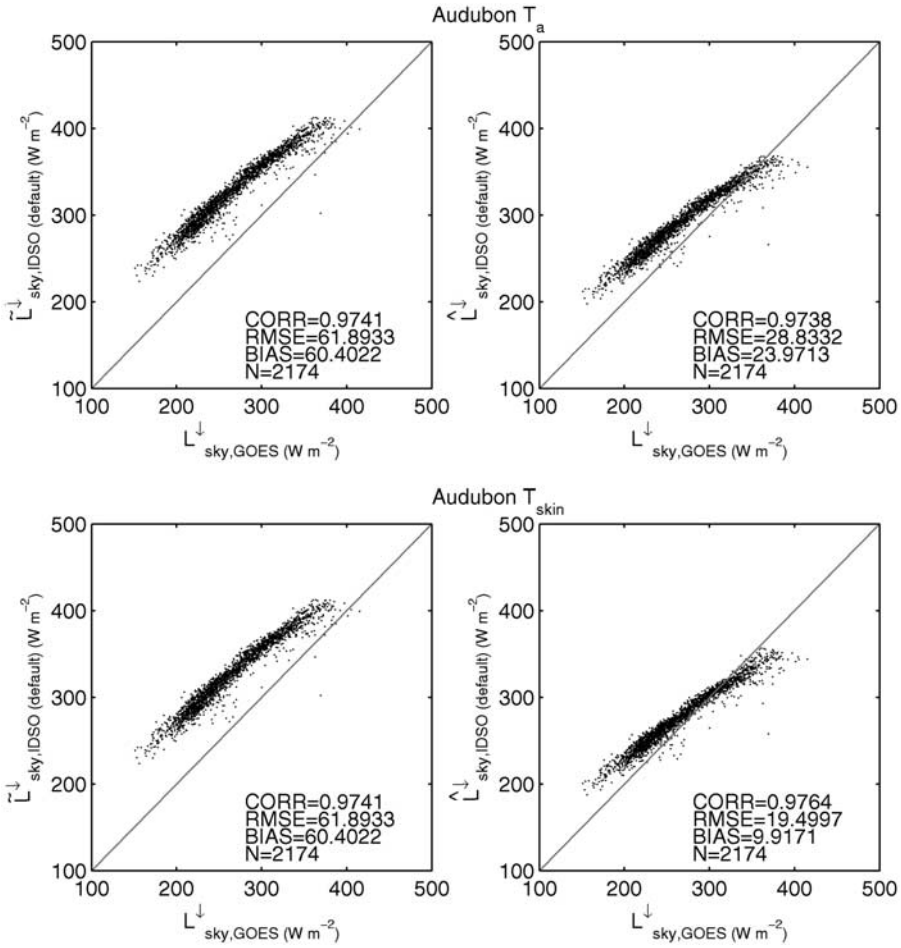

Figure 5. Same as Figure 4 except for the results at Audubon, AZ, with T_{skin} measurements.

strong shortwave radiation can result in T_{skin} to be a few tens of degrees (K) warmer than T_a over the site with sparse vegetation coverage during the warm hours such as summer daytimes (e.g., up to 28.6 K warmer at Audubon, AZ) and thereby the land surface actually emits more longwave radiation than that calculated from T_a. By using the available surface skin temperature at two test sites (Audubon and Fort Peck), the estimated $\hat{L}^{\uparrow}$ becomes more accurate than those from the air temperature (Corr > 0.97, Bias < 11, and RMSE < 20 W m^{-2}). However, Figure 3 shows that during nighttime, the differences between $\hat{L}_a^{\uparrow}$ and $\hat{L}_{skin}^{\uparrow}$ at Audubon reduce substantially (RMSE = 11.62 and Corr = 0.9867). This indicates that we can use nighttime $\hat{L}^{\uparrow}$ for the calibration of clear-sky downwelling longwave radiation where the skin temperature is unavailable, because the calibration of the empirical clear-sky downwelling model only uses nighttime $\hat{L}^{\uparrow}$. Further discussion will follow in section 4.2. Therefore we conclude that surface air temperature is a good substitute for T_{skin} in calculating $L^{\uparrow}$ over vegetated sites in both daytime and nighttime over all regions, but only good in nighttime over sites with sparse vegetation coverage where $L_a^{\uparrow}$ may cause serious underestimation during the warm daytime. Under these conditions, the use of T_{skin} either from ground measurements or from satellite remote sensing is strongly suggested.

4.2. Evaluation of Estimated Clear-Sky Downwelling Longwave Radiation ($\hat{L}_{sky}^{\downarrow}$)

[21] Two comparisons are made to examine the results of $L_{sky}^{\downarrow}$ estimation. In the first comparison, the calculated $\tilde{L}_{sky}^{\downarrow}$ (using the default parameters) and $\hat{L}_{sky}^{\downarrow}$ (using the calibrated parameters) are compared against the observed $L^{\downarrow}$, when the GOES satellite cloudiness index indicates clear sky conditions (cloudiness = 0) at each site. In the second case, biases of $\tilde{L}_{sky}^{\downarrow}$ and $\hat{L}_{sky}^{\downarrow}$ are compared to each other over the (T_a, e_a) bins. Because GOES cloud fraction data are only available for daytime, both comparisons are made for daytime periods.

[22] In Figures 4–6, the $L_{sky}^{\downarrow}$ calculated from calibrated and published parameters ($\hat{L}_{sky}^{\downarrow}$ and $\tilde{L}_{sky}^{\downarrow}$, respectively) is compared with observed $L_{sky}^{\downarrow}$ defined from the GOES clear sky. Figure 4 is for the site without T_{skin} measurements and Figures 5 and 6 are for the sites with T_{skin} measurements. The scattering plots and statistics show that major statistical error measures (RMSE and bias) are improved substantially at all the test sites when parameters were locally calibrated and used. The correlations are also high at all sites (Corr > 0.91). Figures 5 and 6 show that $\hat{L}_{sky}^{\downarrow}$ using T_{skin} also improves the estimations.

[23] Figure 7 illustrates the bias distributions over the (T_a, e_a) bins before and after the calibrations. Clearly, by using the calibrated parameters from nighttime $\hat{L}_{sky}^{\downarrow}$ data, the

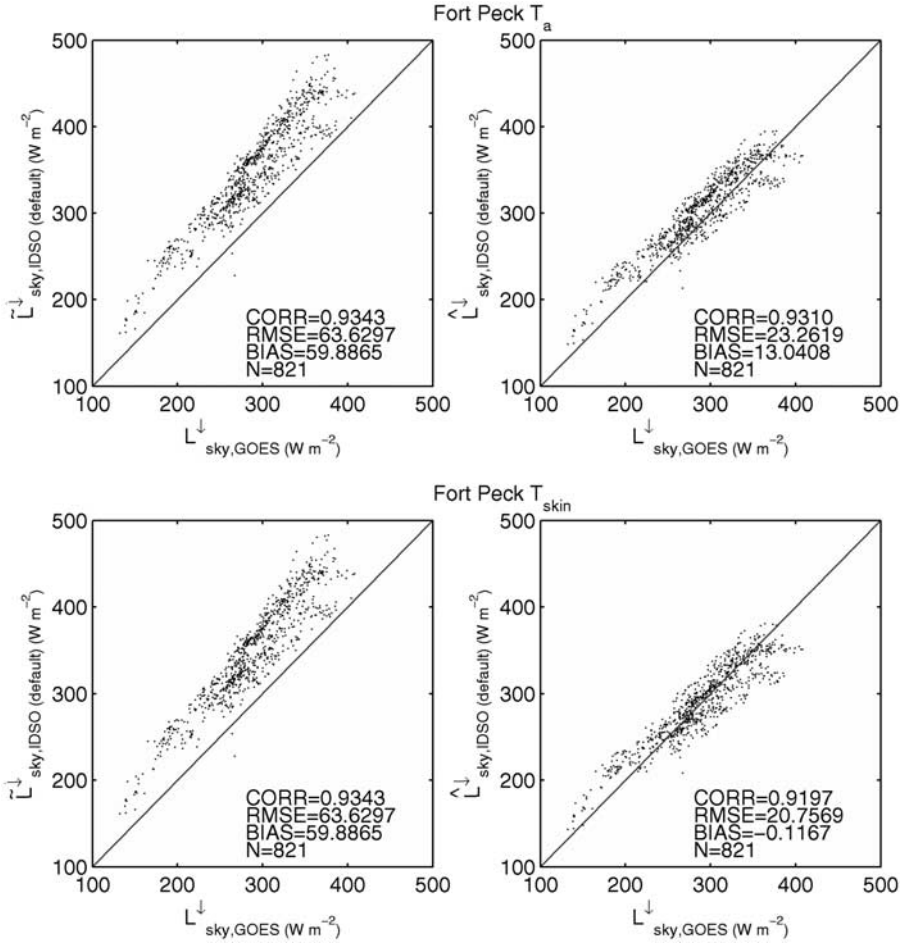

Figure 6. Same as Figure 4 except for the results at Fort Peck, MO, with T_{skin} measurements.

positive biases (up to ±80 W m^{-2}) that exist in $\tilde{L}^{\downarrow}_{sky}$ (Figures 7a, 7c, 7e, and 7g) at most (T_a, e_a) bins are reduced into a much smaller range (±10 W m^{-2}) in $\hat{L}^{\downarrow}_{sky}$ (Figures 7b, 7d, 7f, and 7h). It should be pointed out that the clear sky procedure only uses the nighttime $\hat{L}^{\uparrow}$, and errors associated with daytime results do not affect the calibration of clear-sky model parameters.

[24] However, there are a few bins that experience relatively high biases, particularly on the very high and low temperature ranges. Reasons for this include the limited number of data points and/or possible nonbimodal distribution at some bins. We filtered when data points at each bin are less than 0.2% of total number of data, but this could not completely eliminate small sample bins. Also, the bimodal distribution of $L^{\downarrow}$ might not exist where the number of clear sky hours is limited. In this case, more historical data are required for better calibration. In spite of it, the proposed calibration scheme works at all four sites with acceptable errors.

4.3. Evaluation of Estimated Cloud Downwelling Longwave Radiation ($\hat{L}^{\downarrow}_{cld}$)

[25] From the viewpoint of applications, the error variations in day and nighttimes are interesting. In Figure 8, the diurnal mean bias and RMSE of $\hat{L}^{\downarrow}_{cld}$ at 30-min intervals are plotted according to the Local Standard Time (LST) at each test site. The $\hat{L}^{\downarrow}_{cld}$ data possess small errors (mean bias < 10 W m^{-2}; RMSE < 15 W m^{-2}) during nighttime. During daytime, the errors are more than doubled in comparison with the nighttime data, but still within the ranges acceptable for many applications (mean bias < 22 W m^{-2}; RMSE < 40 W m^{-2}). Considering the error propagated from the previous steps, daytime interpolation of cloud factor seems to provide an alternative approximation when detailed information of cloud conditions is unknown.

4.4. Evaluation of Estimated All-Sky Downwelling Longwave Radiation ($\hat{L}^{\downarrow}$)

[26] In Figure 9, the estimated 30-min all-sky downwelling longwave radiations ($\hat{L}^{\downarrow}$) are depicted against the observed $L^{\downarrow}$ at the test sites. The results show a good agreement between the estimated and observed data at all test sites (Corr > 0.9; RMSE < 27 W m^{-2}; BIAS < 10 W m^{-2}). The major error is related to the estimating step of daytime $\hat{L}^{\downarrow}_{cld}$. When skin temperature is used for $\hat{L}^{\downarrow}$, both Audubon and Fort Peck sites show small improvement in RMSE and Corr, but substantial improvement in Bias. It also shows that the variation range of $L^{\downarrow}$ is around 150–450 W m^{-2} at the test sites. Ignoring $L^{\downarrow}_{cld}$, which is the common cases in offline land surface modeling, will result

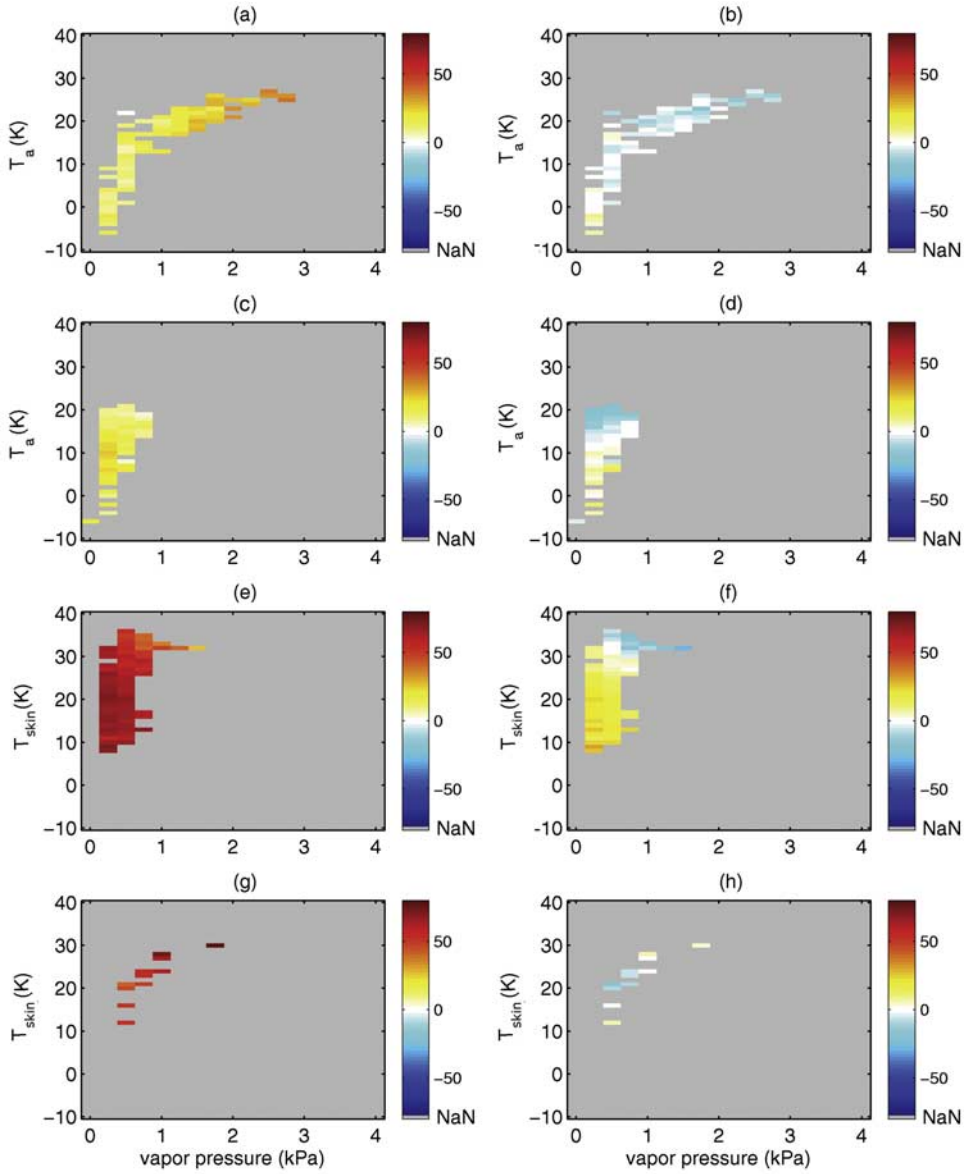

Figure 7. Bias distribution of $\hat{L}^{\downarrow}_{sky}$ over (T_a, e_a) bins for (a and b) Willow Creek, (c and d) Niwot Ridge, (e and f) Audubon, and (g and h) Fort Peck before calibration (Figures 7a, 7c, 7e, and 7g) and after calibration (Figures 7b, 7d, 7f, and 7h).

in a significant energy balance error in the physical processes.

4.5. Evaluation of Estimated Net Solar Radiation ($\hat{S}_n$)

[27] The scatterplots of $\hat{S}_n$ against observations ($S^{\downarrow}-S^{\uparrow}$) at the test sites are shown in Figure 10. The results show high correlations (>0.98), low RMSE (<30 W m^{-2}) and biases (<3 W m^{-2}) when T_{skin} was used for Audubon and Fort Peck sites. It is possible that some positive and negative errors from the previous steps have been canceled, making errors in $\hat{S}_n$ smaller than the sum of errors from $\hat{L}^{\uparrow}$, $\hat{L}^{\downarrow}_{sky}$, and $\hat{L}^{\downarrow}_{cld}$. For example, bias associated with $\hat{L}^{\downarrow}_{sky}$ can be canceled while $\hat{L}^{\downarrow}_{cld}$ is estimated. The mean bias and RMSE of $\hat{S}_n$ during daytime at 30-min time interval are presented in Figure 11. At the four study sites, the maximum diurnal mean bias is ±10 W m^{-2} and the maximum RMSE is 55 W m^{-2} and these errors are relatively small (<10%) with respect to the incident solar radiations at the same time intervals. A comparison between Figures 8 and 11 indicates that large portion of the $\hat{S}_n$ errors comes from the error in $\hat{L}^{\downarrow}_{cld}$. Therefore future improvement of $\hat{L}^{\downarrow}_{cld}$ estimation is expected to effectively reduce the $\hat{S}_n$ errors.

[28] Table 2 summarizes the statistics for the estimations of $\hat{L}^{\uparrow}$, $\hat{L}^{\downarrow}_{\mathrm{sky}}$, $\hat{L}^{\downarrow}$ and $\hat{S}_n$ using the published and calibrated parameters at the test sites.

5. Summary and Conclusions

[29] The lack of long-term, continuous ground radiation measurements covering wide climate and geographic regimes has been a persistent problem in studying land surface processes. A large number of measurement sites set up for diverse research purposes during the last decade have accumulated abundant data that can be used for land surface

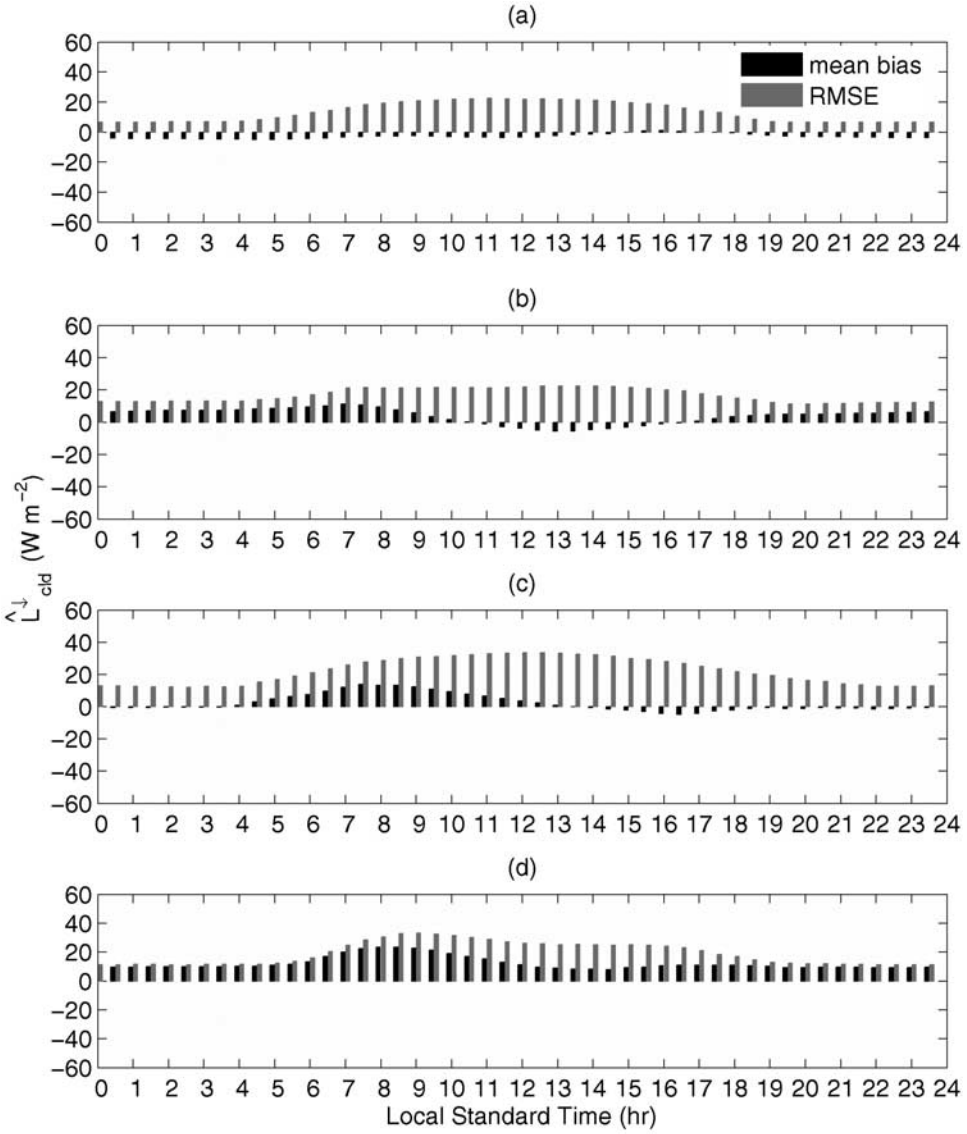

Figure 8. Diurnal mean bias and RMSE of $\hat{L}^{\downarrow}_{cld}$ at 30-min interval for (a) Willow Creek, (b) Niwot Ridge, (c) Audubon, and (d) Fort Peck.

process studies. However, the surface radiation measurements at these sites, in most cases, are limited to a single variable of net radiation or two variables of net radiation and downwelling solar radiation, which are insufficient for many studies that require SW and LW radiation components at the land surface. In this paper, we developed a scheme that improves the accuracy of the empirical models and also estimates the longwave radiation components and the net shortwave radiation. It is an advantage that the method is built solely on the historical net radiation and weather data at an observation site without any additional measurements.

[30] The use of air temperature to estimate upwelling longwave radiation works well in most cases, but it will result in substantial errors at the low vegetated sites during the warm daytime. Under such conditions, it is recommended to use skin temperature. In case the skin temperature T_{skin} is not available from either ground or satellite measurements, it can be estimated from the near-surface air temperature profile simulated by a boundary layer model using the surface weather data [*Businger et al.*, 1971].

[31] The results of the approach were evaluated at four AmeriFlux sites. The statistical errors of all the estimated radiation components at the four sites are relatively low (root mean square error < 30 W m^{-2} and bias < 11 W m^{-2}). This means that the scheme could be, in the future, applied at more field measurement sites covering diverse biomes and climate regimes to produce useful surface radiation data for land surface modeling and ecosystem studies especially for the studies that need hourly and subhourly data. There are two main error sources in the procedure that are subject to improvements. The first is related to the linear interpolation of daytime cloud factor which reflects less realistic diurnal variability of clouds. The second is related to the extraction of nighttime clear-sky data used to calibrate the $\hat{L}^{\downarrow}_{sky}$ estimation model which can deliver uncertainty through the following procedures. We are currently working on these issues for improvements.

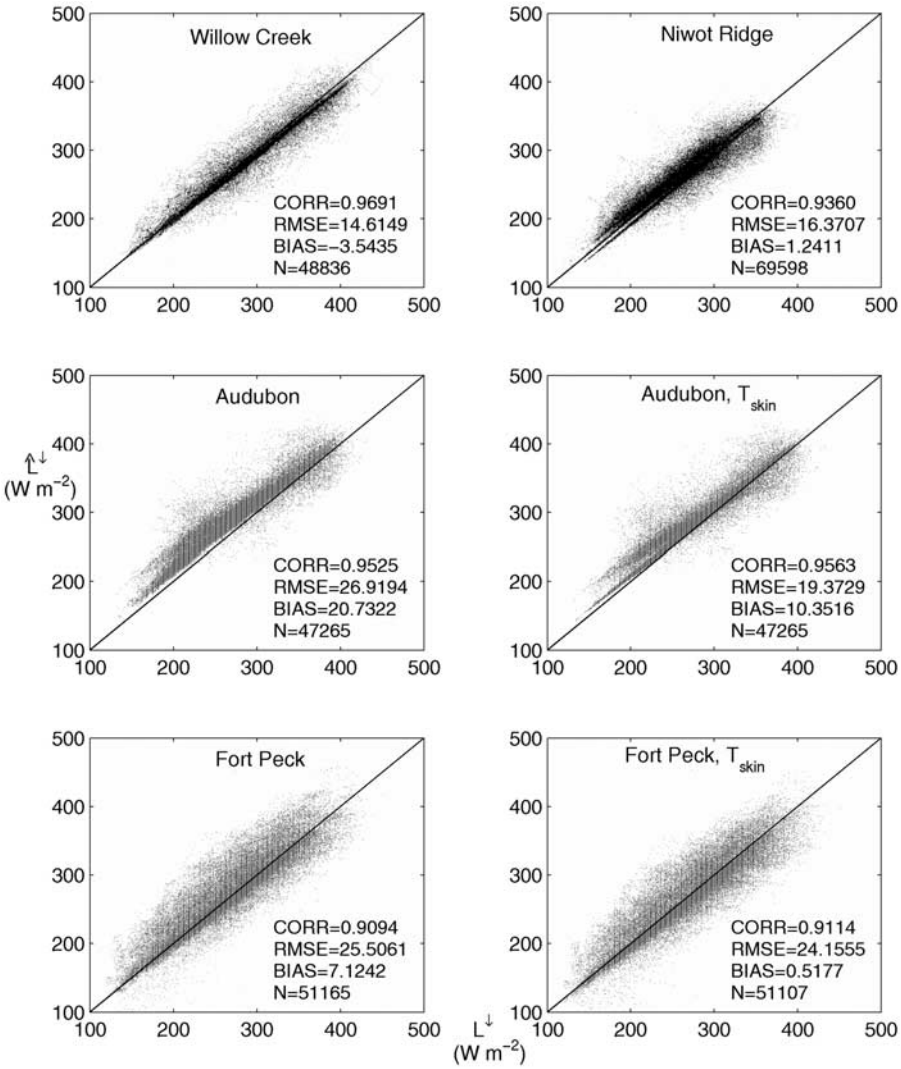

Figure 9. Scatterplots of $L^{\downarrow}$ and $\hat{L}^{\downarrow}$ at the test sites using T_a or T_{skin} (when the measurements are available).

[32] The overall goal of this study is to provide an alternative solution that allows the land surface research community to obtain high-frequency surface radiation data from a large number of existing field measurement sites. This approach is particularly helpful until more accurate information becomes available either from the ground observations or remote sensing products.

Appendix A

[33] Kimball's empirical model for cloud downwelling longwave radiation [*Kimball et al.*, 1982].

$$\hat{L}^{\downarrow}_{cld} = \sum_{i}^{N} \tau_8 A_{ci} \varepsilon_{ci} f_{8i} \sigma T_{ci}^4$$

$$\tau_8 = 1 - \varepsilon_8$$

$$\varepsilon_{8i} = \varepsilon_{8z}(1.4 - 0.4\varepsilon_{8z})$$

$$\varepsilon_{8z} = 0.24 + 2.98 \times 10^{-6} e_a^2 \exp(3000/T_a)$$

$$f_{8i} = -0.6732 + 0.6240 \times 10^{-2} T_{ci} - 0.9140 \times 10^{-5} T_{ci}^2$$

where

N the number of cloud layers, which varies from zero for the clear-sky to 4 for the maximum for-cloud layer case (unitless);

τ_8 the transmittance of the atmosphere in the 8–14 μm window (unitless);

A_{ci} the fraction of the sky covered by the ith cloud layer;

ε_8 the hemispheric 8–14 μm emittance;

ε_{8z} the zenith directional hemispherical emittance (unitless);

ε_{ci} the ith cloud emittance (unitless);

f_{8i} the fraction of blackbody emitted in the 8–14 μm window (unitless);

σ the Stefan-Boltzmann constant (5.6686×10^{-6}) (W m^{-2} K^{-4});

T_{ci} the ith cloud temperature (K);

T_a the air temperature (K);

e_a the vapor pressure (kPa).

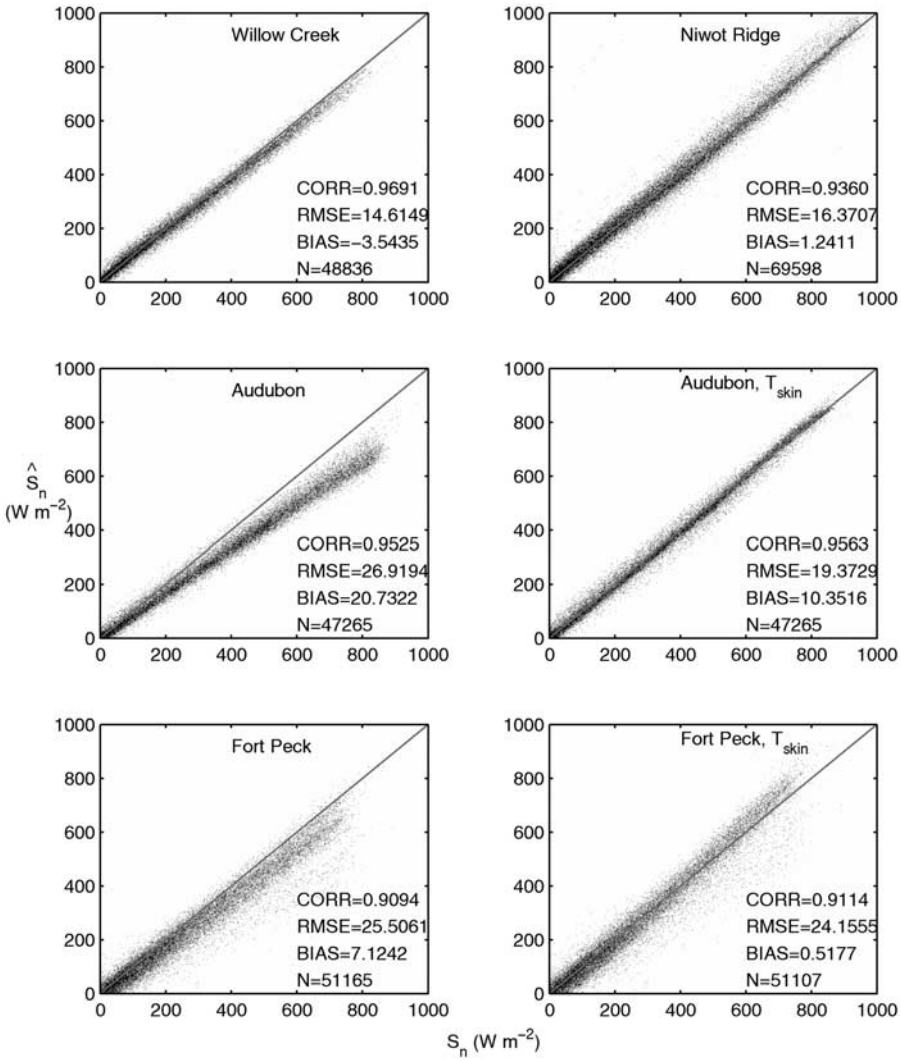

Figure 10. Same as Figure 9 except for $\hat{S}_n$ and S_n.

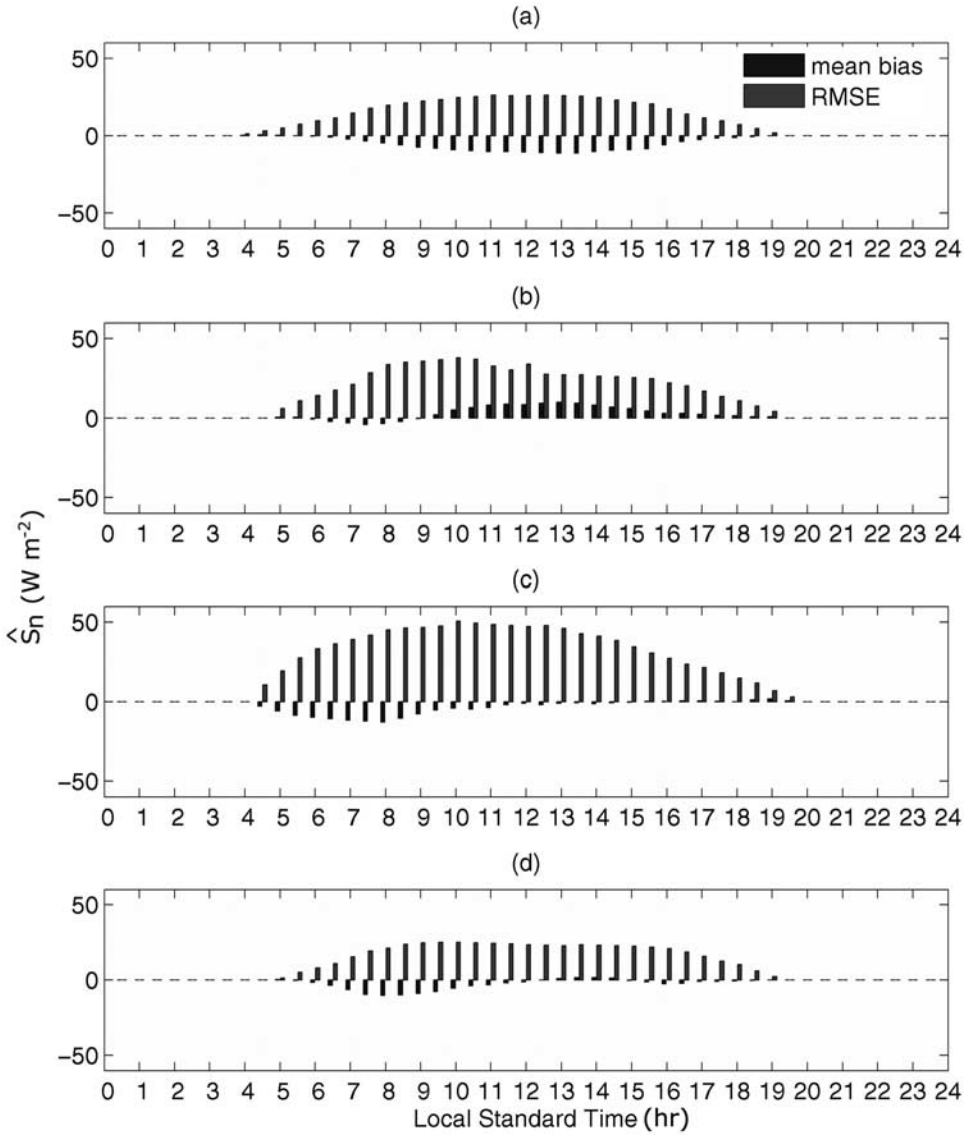

Figure 11. Same as Figure 8 except for $\hat{S}_n$.

Table 2. Calibrated Parameter Values and Error Statistics: Correlation Coefficient (Corr), Root Mean Square Error (RMSE), Bias, and Willmott's Index of Agreement (W_{IA})[a]

	W T_a D	W T_a C	N T_a D	N T_a C	A T_a D	A T_a C	A T_s D	A T_s C	F T_a D	F T_a C	F T_s D	F T_s C
A	0.7000	0.6899	0.7000	0.6182	0.7000	0.6228	0.7000	0.5857	0.7000	0.6056	0.7000	0.5601
B	5.9500	19.9938	5.9500	0.0080	5.9500	19.9682	5.9500	10.1416	5.9500	0.0078	5.9500	0.0038
C	1500	1005	1500	3547	1500	1101	1500	1333	1500	3436	1500	3690
						$\hat{L}^{\uparrow}$						
Corr	0.9934	0.9934	0.9902	0.9902	0.9144	0.9144	0.9989	0.9989	0.9777	0.9777	0.9772	0.9772
RMSE	9.6366	9.6366	10.4246	10.4246	44.7784	44.7784	11.8154	11.8154	22.8698	22.8698	18.2412	18.2412
Bias	−6.9457	−6.9457	−7.8032	−7.8032	−6.9383	−6.9383	10.9944	10.9944	−11.1244	−11.1244	−4.5608	−4.5608
W_{IA}	0.9834	0.9834	0.9678	0.9678	0.7968	0.7968	0.9929	0.9929	0.9497	0.9497	0.9774	0.9774
						$\hat{L}^{\downarrow}_{sky}$						
Corr	0.9755	0.9773	0.9382	0.9295	0.9741	0.9738	0.9741	0.9764	0.9343	0.9310	0.9343	0.9197
RMSE	23.1290	12.5480	20.1642	13.8858	61.8933	28.8332	61.8933	19.4997	63.6297	23.2619	63.6297	20.7569
Bias	18.1381	−2.9775	15.8266	−3.1843	60.4022	23.9713	60.4022	9.9171	59.8865	13.0408	59.8865	−0.1167
W_{IA}	0.9398	0.9707	0.8439	0.8599	0.6524	0.8662	0.6524	0.9187	0.6916	0.8973	0.6916	0.8946
						$\hat{L}^{\downarrow}$						
Corr	0.9621	0.9691	0.9268	0.9360	0.9034	0.9525	0.8852	0.9563	0.8917	0.9094	0.8880	0.9114
RMSE	15.6581	14.6149	17.9187	16.3707	40.5060	26.9194	38.4724	19.3729	33.1982	25.5061	32.6818	24.1555
Bias	−0.4266	−3.5435	4.4318	1.2411	32.4307	20.7322	27.1531	10.3516	16.1290	7.1242	12.6492	0.5177
W_{IA}	0.9616	0.9632	0.9242	0.9323	0.8316	0.9103	0.8413	0.9470	0.8780	0.9076	0.8791	0.9082
						$\hat{S}_n$						
Corr	0.9977	0.9976	0.9964	0.9967	0.9956	0.9968	0.9971	0.9982	0.9853	0.9864	0.9873	0.9882
RMSE	15.2316	12.8101	19.4375	18.9098	69.9148	55.0432	30.0589	15.0542	49.3241	39.7262	33.8754	29.2708
Bias	−4.8276	−2.6291	−1.0802	1.6629	−40.3631	−29.5418	−17.1597	−1.6132	−22.9359	−15.2350	−12.7476	−2.3874
W_{IA}	0.9970	0.9980	0.9977	0.9978	0.9628	0.9785	0.9945	0.9987	0.9717	0.9830	0.9885	0.9992

[a]Unit is W m^{-2}. W, Willow Creek; N, Niwot Ridge; A, Audubon; F, Fort Peck; T_a, air temperature; T_s, skin temperature; D, default parameters; C, calibrated.

[34] In our study, Kimball's multilayer formula is approximated into the single layer model [*Steiner*, 2001] as

$$\hat{L}_{cld}^{\downarrow} = \tau_8 A_c \varepsilon_c f_8 \sigma T_c^4$$

where τ_8 and ε_8 are cloud-independent properties and the cloud temperature (T_c) is estimated by $T_c = T_a - 1.23(T_a - T_d)$, following *Steiner* [2001]. The dew point temperature (T_d) in K, is estimated by rewriting Teten's equation and using the vapor pressure, e_a.

$$T_d = \left(237.3 \ln \frac{e_a}{0.6108}\right) \Big/ \left(17.27 - \ln \frac{e_a}{0.6108}\right)$$

[35] **Acknowledgments.** This work is supported by NASA ESO grant NNG05GA20G and NASA HyDIS grant NAG04GK40G. The surface flux data used in this study were obtained from AmeriFlux website (http://public.ornl.gov/ameriflux/). Following the fair-use policy of AmeriFlux, the authors communicated with and acknowledge scientists at the four AmeriFlux stations for the data: Paul Bolstad and Kenneth Davis (Willow Creek, WI), Russ Monson and Dean Anderson (Niwot Ridge, CO), and Tilden Meyers (Fort Peck, MO, and Audubon, AZ). We thank R. Pinker for making GEWEX/GCIP cloud cover fraction data available and for prereviewing this manuscript with her suggestions. We also thank three anonymous reviewers for their constructive criticism and suggestions.

References

Ångström, A. (1924), Solar and terrestrial radiation, *Q. J. R. Meteorol. Soc.*, *50*, 121–125.

Bechini, L., G. Ducco, M. Donatelli, and A. Stein (2000), Modelling, interpolation and stochastic simulation in space and time of global solar radiation, *Agric. Ecosyst. Environ.*, *81*, 29–42.

Bird, R. E. (1984), A simple, solar spectral model for direct-normal and diffuse horizontal irradiance, *Sol. Energy*, *32*, 461–471.

Businger, J. A., J. C. Wyngaard, Y. Izumi, and E. F. Bradley (1971), Flux-profile relationships in atmospheric surface layer, *J. Atmos. Sci.*, *28*, 181–189.

Duan, Q. Y., S. Sorooshian, and V. Gupta (1992), Effective and efficient global optimization for conceptual rainfall-runoff models, *Water Resour. Res.*, *28*, 1015–1031.

Ehnberg, J. S. G., and M. H. J. Bollen (2005), Simulation of global solar radiation based on cloud observations, *Sol. Energy*, *78*, 157–162.

Gautier, C., and M. Landsfeld (1997), Surface solar radiation flux and cloud radiative forcing for the Atmospheric Radiation Measurement (ARM) Southern Great Plains (SGP): A satellite, surface observations, and radiative transfer model study, *J. Atmos. Sci.*, *54*, 1289–1307.

Gautier, C., G. Diak, and S. Masse (1980), A simple physical model to estimate incident solar-radiation at the surface from goes satellite data, *J. Appl. Meteorol.*, *19*, 1005–1012.

Idso, S. B. (1981), A set of equations for full spectrum and 8- to 14-μm and 10.5- to 12.5-μm thermal radiation from cloudless skies, *Water Resour. Res.*, *17*, 295–304.

Iqbal, M. (1979), Correlation of average diffuse and beam radiation with hours of bright sunshine, *Sol. Energy*, *23*, 169–173.

Iziomon, M. G., H. Mayer, and A. Matzarakis (2003), Downward atmospheric longwave irradiance under clear and cloudy skies: Measurement and parameterization, *J. Atmos. Sol. Terr. Phys.*, *65*, 1107–1116.

Kimball, B. A., S. B. Idso, and J. K. Aase (1982), A model of thermal-radiation from partly cloudy and overcast skies, *Water Resour. Res.*, *18*, 931–936.

Leckner, B. (1978), Spectral distribution of solar-radiation at Earth's surface—Elements of a model, *Sol. Energy*, *20*, 143–150.

Long, C. N., and T. P. Ackerman (2000), Identification of clear skies from broadband pyranometer measurements and calculation of downwelling shortwave cloud effects, *J. Geophys. Res.*, *105*, 15,609–15,626.

Mesinger, F., et al. (2006), North American regional reanalysis, *Bull. Am. Meteorol. Soc.*, *87*, 343–360.

Pinker, R. T., and J. A. Ewing (1985), Modeling surface solar radiation—Model formulation and validation, *J. Clim. Appl. Meteorol.*, *24*, 389–401.

Pinker, R. T., and I. Laszlo (1992), Modeling surface solar irradiance for satellite applications on a global scale, *J. Appl. Meteorol.*, *31*, 194–211.

Pirazzini, R., M. Nardino, A. Orsini, F. Calzolari, T. Georgiadis, and V. Levizzani (2001), Parameterisation of the downward longwave radiation from clear and cloudy skies at Ny-Ålesund (Svalbard), in *IRS' 2000: Current Problems in Atmospheric Radiation*, edited by W. L. Smith and Y. M. Timofeyev, pp. 559–562, A. Deepak Publ., Hampton, Va.

Platnick, S., and J. M. Fontenla (2008), Model calculations of solar spectral irradiance in the 3.7 μm band for Earth remote sensing applications, *J. Appl. Meteorol.*, in press.

Rigollier, C., M. Lefevre, and L. Wald (2004), The method Heliosat-2 for deriving shortwave solar radiation from satellite images, *Sol. Energy*, *77*, 159–169.

Steiner, A. (2001), Effects of land cover change on regional atmospheric chemistry and climate in China, report, pp. 1–27, Int. Inst. for Appl. Syst. Anal., Laxenburg, Austria.

Tarpley, J. D. (1979), Estimating incident solar radiation at the surface from geostationary satellite data, *J. Appl. Meteorol.*, *18*, 1172–1181.

Wild, M., and R. Cechet (2002), Downward longwave radiation in general circulation models: A case study at a semi-arid continental site, *Tellus, Ser. A*, *54*, 330–337.

Willmott, C. J. (1982), Some comments on the evaluation of model performance, *Bull. Am. Meteorol. Soc.*, *63*, 1309–1313.

Yang, K., and T. Koike (2005), A general model to estimate hourly and daily solar radiation for hydrological studies, *Water Resour. Res.*, *41*, W10403, doi:10.1029/2005WR003976.

X. Gao, G.-H. Park, and S. Sorooshian, Department of Civil and Environmental Engineering, University of California, Irvine, CA 92697-2175, USA. (gihyeonp@uci.edu)